DESY-97-147

DESY-97-147

Measurement of Inelastic J/ψ Photoproduction at HERA

hep-ex/9708010 6 Aug 1997

ZEUS Collaboration

Abstract

We present a measurement of the inelastic, non diffractive J/ψ photoproduction cross section in the reaction $e^+p \to e^+\mathrm{J}/\psi X$ with the ZEUS detector at HERA. The J/ψ was identified using both the $\mu^+\mu^-$ and e^+e^- decay channels and events were selected within the range $0.4 < z < 0.9$ ($0.5 < z < 0.9$) for the muon (electron) decay mode, where z is the fraction of the photon energy carried by the J/ψ in the proton rest frame. The cross section, the p_T^2 and the z distributions, after having subtracted the contributions from resolved photon and diffractive proton dissociative processes, are given for the photon-proton centre of mass energy range $50 < W < 180$ GeV; p_T^2 is the square of the J/ψ transverse momentum with respect to the incoming proton beam direction. In the kinematic range $0.4 < z < 0.9$ and $p_T^2 > 1$ GeV^2, NLO calculations of the photon-gluon fusion process based on the colour-singlet model are in good agreement with the data. The predictions of a specific leading order colour-octet model, as formulated to describe the CDF data on J/ψ hadroproduction, are not consistent with the data.

The ZEUS Collaboration

J. Breitweg, M. Derrick, D. Krakauer, S. Magill, D. Mikunas, B. Musgrave, J. Repond, R. Stanek, R.L. Talaga, R. Yoshida, H. Zhang
Argonne National Laboratory, Argonne, IL, USA [p]

M.C.K. Mattingly
Andrews University, Berrien Springs, MI, USA

F. Anselmo, P. Antonioli, G. Bari, M. Basile, L. Bellagamba, D. Boscherini, A. Bruni, G. Bruni, G. Cara Romeo, G. Castellini[1], L. Cifarelli[2], F. Cindolo, A. Contin, M. Corradi, S. De Pasquale, I. Gialas[3], P. Giusti, G. Iacobucci, G. Laurenti, G. Levi, A. Margotti, T. Massam, R. Nania, F. Palmonari, A. Pesci, A. Polini, F. Ricci, G. Sartorelli, Y. Zamora Garcia[4], A. Zichichi
University and INFN Bologna, Bologna, Italy [f]

C. Amelung, A. Bornheim, I. Brock, K. Coböken, J. Crittenden, R. Deffner, M. Eckert, M. Grothe, H. Hartmann, K. Heinloth, L. Heinz, E. Hilger, H.-P. Jakob, U.F. Katz, R. Kerger, E. Paul, M. Pfeiffer, Ch. Rembser[5], J. Stamm, R. Wedemeyer[6], H. Wieber
Physikalisches Institut der Universität Bonn, Bonn, Germany [c]

D.S. Bailey, S. Campbell-Robson, W.N. Cottingham, B. Foster, R. Hall-Wilton, M.E. Hayes, G.P. Heath, H.F. Heath, D. Piccioni, D.G. Roff, R.J. Tapper
H.H. Wills Physics Laboratory, University of Bristol, Bristol, U.K. [o]

M. Arneodo[7], R. Ayad, M. Capua, A. Garfagnini, L. Iannotti, M. Schioppa, G. Susinno
Calabria University, Physics Dept.and INFN, Cosenza, Italy [f]

J.Y. Kim, J.H. Lee, I.T. Lim, M.Y. Pac[8]
Chonnam National University, Kwangju, Korea [h]

A. Caldwell[9], N. Cartiglia, Z. Jing, W. Liu, B. Mellado, J.A. Parsons, S. Ritz[10], S. Sampson, F. Sciulli, P.B. Straub, Q. Zhu
Columbia University, Nevis Labs., Irvington on Hudson, N.Y., USA [q]

P. Borzemski, J. Chwastowski, A. Eskreys, Z. Jakubowski, M.B. Przybycień, M. Zachara, L. Zawiejski
Inst. of Nuclear Physics, Cracow, Poland [j]

L. Adamczyk[11], B. Bednarek, M. Bukowy, K. Jeleń, D. Kisielewska, T. Kowalski, M. Przybycień, E. Rulikowska-Zarębska, L. Suszycki, J. Zając
Faculty of Physics and Nuclear Techniques, Academy of Mining and Metallurgy, Cracow, Poland [j]

Z. Duliński, A. Kotański
Jagellonian Univ., Dept. of Physics, Cracow, Poland [k]

G. Abbiendi[12], L.A.T. Bauerdick, U. Behrens, H. Beier, J.K. Bienlein, G. Cases[13], O. Deppe, K. Desler, G. Drews, U. Fricke, D.J. Gilkinson, C. Glasman, P. Göttlicher, J. Große-Knetter, T. Haas, W. Hain, D. Hasell, K.F. Johnson[14], M. Kasemann, W. Koch, U. Kötz, H. Kowalski, J. Labs, L. Lindemann, B. Löhr, M. Löwe[15], O. Mańczak, J. Milewski, T. Monteiro[16], J.S.T. Ng[17], D. Notz, K. Ohrenberg[18], I.H. Park[19], A. Pellegrino, F. Pelucchi, K. Piotrzkowski, M. Roco[20], M. Rohde, J. Roldán, J.J. Ryan, A.A. Savin, U. Schneekloth, F. Selonke, B. Surrow, E. Tassi, T. Voß[21], D. Westphal, G. Wolf, U. Wollmer[22], C. Youngman, A.F. Żarnecki, W. Zeuner
Deutsches Elektronen-Synchrotron DESY, Hamburg, Germany

B.D. Burow, H.J. Grabosch, A. Meyer, S. Schlenstedt
DESY-IfH Zeuthen, Zeuthen, Germany

G. Barbagli, E. Gallo, P. Pelfer
University and INFN, Florence, Italy [f]

G. Maccarrone, L. Votano
INFN, Laboratori Nazionali di Frascati, Frascati, Italy [f]

A. Bamberger, S. Eisenhardt, P. Markun, T. Trefzger[23], S. Wölfle
Fakultät für Physik der Universität Freiburg i.Br., Freiburg i.Br., Germany [c]

J.T. Bromley, N.H. Brook, P.J. Bussey, A.T. Doyle, D.H. Saxon, L.E. Sinclair, E. Strickland, M.L. Utley[24], R. Waugh, A.S. Wilson
Dept. of Physics and Astronomy, University of Glasgow, Glasgow, U.K. [o]

I. Bohnet, N. Gendner, U. Holm, A. Meyer-Larsen, H. Salehi, K. Wick
Hamburg University, I. Institute of Exp. Physics, Hamburg, Germany [c]

L.K. Gladilin[25], D. Horstmann, D. Kçira, R. Klanner, E. Lohrmann, G. Poelz, W. Schott[26], F. Zetsche
Hamburg University, II. Institute of Exp. Physics, Hamburg, Germany [c]

T.C. Bacon, I. Butterworth, J.E. Cole, V.L. Harris, G. Howell, B.H.Y. Hung, L. Lamberti[27], K.R. Long, D.B. Miller, N. Pavel, A. Prinias[28], J.K. Sedgbeer, D. Sideris, A.F. Whitfield[29]
Imperial College London, High Energy Nuclear Physics Group, London, U.K. [o]

U. Mallik, S.M. Wang, J.T. Wu
University of Iowa, Physics and Astronomy Dept., Iowa City, USA [p]

P. Cloth, D. Filges
Forschungszentrum Jülich, Institut für Kernphysik, Jülich, Germany

J.I. Fleck[5], T. Ishii, M. Kuze, M. Nakao, K. Tokushuku, S. Yamada, Y. Yamazaki[30]
Institute of Particle and Nuclear Studies, KEK, Tsukuba, Japan [g]

S.H. An, S.B. Lee, S.W. Nam[31], H.S. Park, S.K. Park
Korea University, Seoul, Korea [h]

F. Barreiro, J.P. Fernández, G. García, R. Graciani, J.M. Hernández, L. Hervás[5], L. Labarga, M. Martínez, J. del Peso, J. Puga, J. Terrón[32], J.F. de Trocóniz
Univer. Autónoma Madrid, Depto de Física Teórica, Madrid, Spain [n]

F. Corriveau, D.S. Hanna, J. Hartmann, L.W. Hung, J.N. Lim, W.N. Murray, A. Ochs, M. Riveline, D.G. Stairs, M. St-Laurent, R. Ullmann
McGill University, Dept. of Physics, Montréal, Québec, Canada [a], [b]

T. Tsurugai
Meiji Gakuin University, Faculty of General Education, Yokohama, Japan

V. Bashkirov, B.A. Dolgoshein, A. Stifutkin
Moscow Engineering Physics Institute, Moscow, Russia [l]

G.L. Bashindzhagyan, P.F. Ermolov, Yu.A. Golubkov, L.A. Khein, N.A. Korotkova, I.A. Korzhavina, V.A. Kuzmin, O.Yu. Lukina, A.S. Proskuryakov, L.M. Shcheglova[33], A.N. Solomin[33], S.A. Zotkin
Moscow State University, Institute of Nuclear Physics, Moscow, Russia [m]

C. Bokel, M. Botje, N. Brümmer, F. Chlebana[20], J. Engelen, P. Kooijman, A. van Sighem, H. Tiecke, N. Tuning, W. Verkerke, J. Vossebeld, M. Vreeswijk[5], L. Wiggers, E. de Wolf
NIKHEF and University of Amsterdam, Amsterdam, Netherlands [i]

D. Acosta, B. Bylsma, L.S. Durkin, J. Gilmore, C.M. Ginsburg, C.L. Kim, T.Y. Ling, P. Nylander, T.A. Romanowski[34]
Ohio State University, Physics Department, Columbus, Ohio, USA [p]

H.E. Blaikley, R.J. Cashmore, A.M. Cooper-Sarkar, R.C.E. Devenish, J.K. Edmonds, N. Harnew,
M. Lancaster[35], J.D. McFall, C. Nath, V.A. Noyes[28], A. Quadt, O. Ruske, J.R. Tickner, H. Uijterwaal,
R. Walczak, D.S. Waters
Department of Physics, University of Oxford, Oxford, U.K. [o]

A. Bertolin, R. Brugnera, R. Carlin, F. Dal Corso, M. De Giorgi, U. Dosselli, S. Limentani, M. Morandin, M. Posocco, L. Stanco, R. Stroili, C. Voci, F. Zuin
Dipartimento di Fisica dell' Università and INFN, Padova, Italy [f]

J. Bulmahn, R.G. Feild[36], B.Y. Oh, J.R. Okrasiński, J.J. Whitmore
Pennsylvania State University, Dept. of Physics, University Park, PA, USA [q]

Y. Iga
Polytechnic University, Sagamihara, Japan [g]

G. D'Agostini, G. Marini, A. Nigro, M. Raso
Dipartimento di Fisica, Univ. 'La Sapienza' and INFN, Rome, Italy [f]

J.C. Hart, N.A. McCubbin, T.P. Shah
Rutherford Appleton Laboratory, Chilton, Didcot, Oxon, U.K. [o]

D. Epperson, C. Heusch, J.T. Rahn, H.F.-W. Sadrozinski, A. Seiden, D.C. Williams
University of California, Santa Cruz, CA, USA [p]

O. Schwarzer, A.H. Walenta
Fachbereich Physik der Universität-Gesamthochschule Siegen, Germany [c]

H. Abramowicz[37], G. Briskin, S. Dagan[37], S. Kananov[37], A. Levy[37]
Raymond and Beverly Sackler Faculty of Exact Sciences, School of Physics, Tel-Aviv University,
Tel-Aviv, Israel [e]

T. Abe, T. Fusayasu, M. Inuzuka, K. Nagano, I. Suzuki, K. Umemori, T. Yamashita
Department of Physics, University of Tokyo, Tokyo, Japan [g]

R. Hamatsu, T. Hirose, K. Homma, S. Kitamura[38], T. Matsushita, K. Yamauchi
Tokyo Metropolitan University, Dept. of Physics, Tokyo, Japan [g]

R. Cirio, M. Costa, M.I. Ferrero, S. Maselli, V. Monaco, C. Peroni, M.C. Petrucci, R. Sacchi, A. Solano, A. Staiano
Università di Torino, Dipartimento di Fisica Sperimentale and INFN, Torino, Italy [f]

M. Dardo
II Faculty of Sciences, Torino University and INFN - Alessandria, Italy [f]

D.C. Bailey, M. Brkic, C.-P. Fagerstroem, G.F. Hartner, K.K. Joo, G.M. Levman, J.F. Martin, R.S. Orr, S. Polenz, C.R. Sampson, D. Simmons, R.J. Teuscher[5]
University of Toronto, Dept. of Physics, Toronto, Ont., Canada [a]

J.M. Butterworth, C.D. Catterall, T.W. Jones, P.B. Kaziewicz, J.B. Lane, R.L. Saunders, J. Shulman, M.R. Sutton
University College London, Physics and Astronomy Dept., London, U.K. [o]

B. Lu, L.W. Mo
Virginia Polytechnic Inst. and State University, Physics Dept., Blacksburg, VA, USA [q]

J. Ciborowski, G. Grzelak[39], M. Kasprzak, K. Muchorowski[40], R.J. Nowak, J.M. Pawlak, R. Pawlak, T. Tymieniecka, A.K. Wróblewski, J.A. Zakrzewski
Warsaw University, Institute of Experimental Physics, Warsaw, Poland [j]

M. Adamus
Institute for Nuclear Studies, Warsaw, Poland [j]

C. Coldewey, Y. Eisenberg[37], D. Hochman, U. Karshon[37], D. Revel[37]
Weizmann Institute, Department of Particle Physics, Rehovot, Israel [d]

W.F. Badgett, D. Chapin, R. Cross, S. Dasu, C. Foudas, R.J. Loveless, S. Mattingly, D.D. Reeder, W.H. Smith, A. Vaiciulis, M. Wodarczyk
University of Wisconsin, Dept. of Physics, Madison, WI, USA [p]

S. Bhadra, W.R. Frisken, M. Khakzad, W.B. Schmidke
York University, Dept. of Physics, North York, Ont., Canada [a]

[1] also at IROE Florence, Italy
[2] now at Univ. of Salerno and INFN Napoli, Italy
[3] now at Univ. of Crete, Greece
[4] supported by Worldlab, Lausanne, Switzerland
[5] now at CERN
[6] retired
[7] also at University of Torino and Alexander von Humboldt Fellow at University of Hamburg
[8] now at Dongshin University, Naju, Korea
[9] also at DESY
[10] Alfred P. Sloan Foundation Fellow
[11] supported by the Polish State Committee for Scientific Research, grant No. 2P03B14912
[12] supported by an EC fellowship number ERBFMBICT 950172
[13] now at SAP A.G., Walldorf
[14] visitor from Florida State University
[15] now at ALCATEL Mobile Communication GmbH, Stuttgart
[16] supported by European Community Program PRAXIS XXI
[17] now at DESY-Group FDET
[18] now at DESY Computer Center
[19] visitor from Kyungpook National University, Taegu, Korea, partially supported by DESY
[20] now at Fermi National Accelerator Laboratory (FNAL), Batavia, IL, USA
[21] now at NORCOM Infosystems, Hamburg
[22] now at Oxford University, supported by DAAD fellowship HSP II-AUFE III
[23] now at ATLAS Collaboration, Univ. of Munich
[24] now at Clinical Operational Research Unit, University College, London
[25] on leave from MSU, supported by the GIF, contract I-0444-176.07/95
[26] now a self-employed consultant
[27] supported by an EC fellowship
[28] PPARC Post-doctoral Fellow
[29] now at Conduit Communications Ltd., London, U.K.
[30] supported by JSPS Postdoctoral Fellowships for Research Abroad
[31] now at Wayne State University, Detroit
[32] partially supported by Comunidad Autonoma Madrid
[33] partially supported by the Foundation for German-Russian Collaboration DFG-RFBR (grant nos 436 RUS 113/248/3 and 436 RUS 113/248/2)
[34] now at Department of Energy, Washington
[35] now at Lawrence Berkeley Laboratory, Berkeley, CA, USA
[36] now at Yale University, New Haven, CT
[37] supported by a MINERVA Fellowship
[38] present address: Tokyo Metropolitan College of Allied Medical Sciences, Tokyo 116, Japan
[39] supported by the Polish State Committee for Scientific Research, grant No. 2P03B09308
[40] supported by the Polish State Committee for Scientific Research, grant No. 2P03B09208

[a] supported by the Natural Sciences and Engineering Research Council of Canada (NSERC)
[b] supported by the FCAR of Québec, Canada
[c] supported by the German Federal Ministry for Education and Science, Research and Technology (BMBF), under contract numbers 057BN19P, 057FR19P, 057HH19P, 057HH29P, 057SI75I
[d] supported by the MINERVA Gesellschaft für Forschung GmbH, the German Israeli Foundation, and the U.S.-Israel Binational Science Foundation
[e] supported by the German Israeli Foundation, and by the Israel Science Foundation
[f] supported by the Italian National Institute for Nuclear Physics (INFN)
[g] supported by the Japanese Ministry of Education, Science and Culture (the Monbusho) and its grants for Scientific Research
[h] supported by the Korean Ministry of Education and Korea Science and Engineering Foundation
[i] supported by the Netherlands Foundation for Research on Matter (FOM)
[j] supported by the Polish State Committee for Scientific Research, grant No. 115/E-343/SPUB/P03/002/97, 2P03B10512, 2P03B10612, 2P03B14212, 2P03B10412
[k] supported by the Polish State Committee for Scientific Research (grant No. 2P03B08308) and Foundation for Polish-German Collaboration
[l] partially supported by the German Federal Ministry for Education and Science, Research and Technology (BMBF)
[m] supported by the Fund for Fundamental Research of Russian Ministry for Science and Education and by the German Federal Ministry for Education and Science, Research and Technology (BMBF)
[n] supported by the Spanish Ministry of Education and Science through funds provided by CICYT
[o] supported by the Particle Physics and Astronomy Research Council
[p] supported by the US Department of Energy
[q] supported by the US National Science Foundation

1 Introduction

The inelastic reaction $e^+p \to e^+\mathrm{J}/\psi X$ in the photoproduction regime ($Q^2 \approx 0$ GeV^2, where Q^2 is the photon virtuality) is thought to proceed via direct photon-gluon fusion, diffractive proton dissociation or resolved photon processes. These three possibilities are shown in Fig. 1. In this paper we are primarily interested in the contribution from the direct photon-gluon fusion process, shown in Fig. 1a, for which full next-to-leading order (NLO) QCD calculations are available [1], in the framework of the colour-singlet model [2]. The predicted cross section is sensitive to the gluon density in the proton at an energy scale corresponding approximately to the heavy quark mass. Perturbative QCD calculations using as input the parton densities extracted from other processes can therefore provide a consistency test for QCD. In inelastic J/ψ photoproduction the concepts of direct and resolved photon contributions remain distinct up to the NLO level. This is due to the particular spin and colour state projection involved in the calculation, which makes this reaction different from those involving light and open heavy quark production, in which only the sum of direct and resolved terms is unambiguously defined at NLO [3].

The different processes in Fig. 1 can be distinguished by means of the inelasticity variable z, the fraction of the photon energy carried by the J/ψ in the proton rest frame [4]. The diffractive proton dissociation process dominates the high z region ($z > 0.9$), the photon-gluon fusion the intermediate z region, while the resolved photon process is dominant in the low z region. There are also differences in the p_T distribution, p_T being the J/ψ transverse momentum with respect to the incoming proton beam direction. Compared to photon-gluon fusion and resolved photon processes the diffractive reaction produces J/ψ mesons with relatively low p_T ($p_T \lesssim 1$ GeV).

The direct photon-gluon fusion process is described in [1] in the framework of the colour-singlet model [2], in which the initial state photon and gluon interact giving a final state $c\bar{c}$ pair with the J/ψ quantum numbers through the emission of a hard gluon in the final state ($\gamma + g_1 \to \mathrm{J}/\psi + g_2$). When a similar model was used to study J/ψ hadroproduction [5] at the Tevatron, the predictions, at lowest order in the strong coupling constant α_s, underestimated the data [6] by about one order of magnitude. The measured cross section could be explained in part by adding colour-octet contributions [7]. In this case the $c\bar{c}$ pair is produced in a colour-octet state (short distance process) and later binds to form a J/ψ (long distance process). While the short distance terms are calculable through perturbative QCD, the long distance terms are nonperturbative and have to be determined from the data themselves. It is therefore interesting to look for evidence of the octet mechanism at HERA, where it is expected to contribute at high z [8].

Previous fixed target experiments both in the photoproduction [9, 10] and in the electroproduction [11, 12, 13, 14] regime measured the inelastic J/ψ cross section for photon-proton centre of mass energies, W, between 10 and 20 GeV. The H1 Collaboration [15] has published results on inelastic J/ψ production in the interval $30 < W < 150$ GeV.

In the following sections, after a brief description of the experimental conditions, we discuss the kinematics of inelastic J/ψ production and the criteria used to select events in the region where the direct photon-gluon fusion process is dominant. We then evaluate the cross section for this process in the range $50 < W < 180$ GeV and $0.4 < z < 0.9$

for the muon case and in $90 < W < 180$ GeV, $0.5 < z < 0.9$ for the electron case. The cross section is extrapolated to $z = 0$ assuming the direct photon-gluon fusion model. Comparisons with NLO calculations are discussed in section 8 for the restricted kinematic range $z < 0.8$ and $p_T^2 > 1$ GeV^2, where the calculations are reliable.

The data were collected in 1994 and correspond to an integrated luminosity of 2.99 ± 0.05 pb^{-1}.

2 Experimental Conditions

2.1 HERA

During 1994 HERA operated with a proton beam energy of 820 GeV and a positron beam energy of 27.5 GeV. There were 153 colliding proton and positron bunches together with an additional 17 unpaired proton bunches and 15 unpaired positron bunches. The root mean square (rms) proton bunch length was approximately 20 cm while the positron bunch length was small in comparison. The time between bunch crossings was 96 ns. The typical instantaneous luminosity was 1.5×10^{30} cm^{-2} s^{-1}.

2.2 The ZEUS Detector

The main ZEUS detector components used in this analysis are outlined below. A detailed description of the ZEUS detector can be found elsewhere [16]. In the following the ZEUS coordinate system is used, the Z axis of which is coincident with the nominal proton beam axis, the X axis is horizontal and points towards the centre of HERA and the Y axis completes a right-handed coordinate system. The origin of the coordinates is at the nominal interaction point.

The momenta and trajectories of charged particles are reconstructed using the vertex detector (VXD) [17] and the central tracking detector (CTD) [18]. The VXD and the CTD are cylindrical drift chambers covering the angular region $15^o < \theta < 164^o$ (where θ is the polar angle with respect to the proton direction). The chambers are located in a magnetic field of 1.43 T produced by a thin superconducting solenoid.

The high resolution uranium-scintillator calorimeter (CAL) [19] surrounding the coil is divided into three parts, the forward calorimeter (FCAL), the barrel calorimeter (BCAL) and the rear calorimeter (RCAL). They cover polar angles from 2.6^o to 36.7^o, 36.7^o to 129.1^o, and 129.1^o to 176.2^o, respectively. Each part consists of towers which are longitudinally subdivided into electromagnetic (EMC) and hadronic (HAC) readout cells. The CAL also provides a time resolution of better than 1 ns for energy deposits greater than 4.5 GeV, and this timing is used for background rejection.

The hadron electron separator (HES) [20] consists of silicon detectors 400 μm thick. In the 1994 running period only the rear part (RHES) was operational. The RHES is located in the RCAL at a depth of 3.3 radiation lengths, covering an area of about 10 m^2. Each

silicon pad has an area of 28.9 x 30.5 mm^2, providing a spatial resolution of about 9 mm for a single hit pad. If more than one adjacent pad is hit by a shower, a cluster consisting of at most 3 x 3 pads around the most energetic pad is considered. This allows a more precise reconstruction of the position with a resolution of about 5 mm for energies greater than 5 GeV. The RHES measures the energy deposited by charged particles near the maximum of an electromagnetic shower.

The muon detectors [21], situated outside the calorimeter, consist of limited streamer tube (LST) planes with the inner chambers in front of the magnetised iron yoke and the outer chambers behind it. Owing to the low momentum of the J/ψ decay muons, only the inner chambers (BMUI and RMUI) were used in the present analysis. The BMUI and the RMUI cover the polar angular ranges $34^o < \theta < 135^o$ and $134^o < \theta < 171^o$, respectively.

The luminosity is determined from the rate of events due to the Bethe-Heitler process $e^+p \to e^+\gamma p$, where the photon is measured by the calorimeter of the luminosity detector (LUMI) located in the HERA tunnel in the direction of the outgoing positron beam [22]. For the measurements presented in this paper the luminosity was determined with a precision of 1.5%.

3 Kinematics

Schematic diagrams for the reaction:

$$e^+(k)p(P) \to e^+(k')\mathrm{J}/\psi(p_{J/\psi})X, \tag{1}$$

where each symbol in parentheses denotes the four-momentum of the corresponding particle, are shown in Fig. 1.

The kinematics of the inclusive scattering of unpolarised positrons and protons is described by the positron-proton centre of mass energy squared (s) and any two of the following variables:

- $Q^2 = -q^2 = -(k - k')^2$, the negative four-momentum squared of the exchanged photon;
- $y = (q \cdot P)/(k \cdot P)$, the fraction of the positron energy transferred to the hadronic final state in the rest frame of the initial state proton;
- $W^2 = (q + P)^2 = -Q^2 + 2y(k \cdot P) + M_p^2 \approx ys$, the centre of mass energy squared of the photon-proton system, where M_p is the proton mass.

Restricting our measurement to photoproduction events where the outgoing positron is not in the CAL acceptance, the Q^2 value ranges from the kinematic minimum $Q^2_{min} = M_e^2 y^2/(1-y) \sim 10^{-10}$ GeV^2, where M_e is the electron mass, to the value at which the scattered positron starts to be observed in the uranium calorimeter, $Q^2_{max} \sim 4$ GeV^2. The median Q^2 is approximately 10^{-4} GeV^2.

The value of y was determined by the Jacquet-Blondel formula [23]:

$$y \simeq y_{JB} = \frac{\sum_i (E_i - p_{Z_i})}{2E_e}, \tag{2}$$

where the sum runs over all the calorimeter cells and E_i is the cell energy, p_{Z_i} is equal to $E_i \cos\theta_i$, where θ_i is the polar angle of the cell measured with respect to the nominal vertex, and E_e is the incoming positron energy. The value of W is determined from the relation $W^2 = y_{JB}s$.

For reaction (1) the inelasticity variable, z, is defined by

$$z = \frac{P \cdot p_{J/\psi}}{P \cdot q} \simeq \frac{(E_{J/\psi} - p_{Z_{J/\psi}})}{2yE_e}, \tag{3}$$

where $E_{J/\psi}$ is the J/ψ energy and $p_{Z_{J/\psi}}$ is its momentum component along the Z direction. In the proton rest frame, z is equal to $\frac{E_{J/\psi}}{E_\gamma}$, where E_γ is the photon energy. Experimentally z is estimated from:

$$z = \frac{(E_{J/\psi} - p_{Z_{J/\psi}})}{2y_{JB}E_e} = \frac{(E_{J/\psi} - p_{Z_{J/\psi}})}{\sum_i (E_i - p_{Z_i})}. \tag{4}$$

In the estimations of y_{JB} and z, using equations (2) and (4), the contribution of the two leptons from the J/ψ decay was accounted for by including in the sum their momenta as measured in the central tracking detectors while discarding their calorimetric deposits.

4 Event Selection

The selection of the muon and electron decay channels followed different paths, except for the common veto requirements at the first level trigger (FLT), which reject proton-gas background events occuring upstream of the nominal interaction point and which are therefore out of time with respect to the e^+p interactions.

4.1 Muon Mode

The candidates for the J/$\psi \to \mu^+\mu^-$ channel were selected using the three level ZEUS trigger system. At the FLT a coincidence between track segments in the CTD, energy deposits in the CAL and hits in the BMUI or RMUI was used to select muon candidates. The CAL was divided in $Z - \phi$ regions (ϕ being the azimuthal angle around the Z axis) associated with the corresponding zones of the barrel and rear muon chambers. A signal above threshold in one of the CAL regions in conjunction with a hit in the associated barrel or rear muon chamber defined a CAL-BMUI/RMUI match. This regional matching was demanded together with the requirement of tracks in the CTD pointing to the nominal vertex.

At the second level trigger (SLT), the total energy in the calorimeter ($E_{Tot} = \Sigma_i E_i$) and the Z component of the momentum ($\Sigma_i p_{Z_i} = \Sigma_i E_i \cos\theta_i$) were calculated. The sums

run over all calorimeter cells i with an energy, E_i, above threshold at a polar angle, θ_i, measured with respect to the nominal vertex. In order to remove proton-gas interactions, events with the ratio $\Sigma_i p_{Z_i}/E_{Tot}$ greater than 0.96 were rejected. Part of the cosmic ray background was rejected at the SLT by using the time difference of the energy deposits in the upper and the lower halves of the calorimeter.

At the third level trigger (TLT) a muon candidate was selected when a track found in the CTD matched both a cluster with a calorimeter energy deposit consistent with the passage of a minimum ionising particle (a m.i.p. cluster [1]) and a track in the inner muon chambers. An event containing a muon candidate in the rear (barrel) region was accepted if the (transverse) momentum of the CTD track exceeded 1 GeV.

The TLT algorithm was again applied in the offline analysis, but now the results of the full event reconstruction were used. The tracks corresponding to the two muons from the J/ψ decay had to satisfy the following criteria, where the subscript 1 denotes the triggering muon and the subscript 2 the other muon and p indicates the momentum of a muon and p_t its transverse momentum:

- $p_1 > 1$ GeV (rear region); $p_{t1} > 1$ GeV (barrel region);
- $p_2 > 1$ GeV;
- $p_{t1} + p_{t2} > 2.8$ GeV;
- pseudorapidities[2] $|\eta_{1,2}| < 1.75$;
- the second muon track has to match a m.i.p. cluster in the CAL.

Cosmic rays were rejected by requiring that the two muon tracks were not collinear: events with $\Omega > 174^o$ were rejected, where Ω is the angle between the two tracks at the interaction point.

The final inelastic data sample was defined by requiring an energy deposit greater than 1 GeV in a cone of 35^o around the forward direction (excluding the calorimeter deposits due to the muons). Elastically produced J/ψ mesons were thus excluded. The data were further restricted to the W interval 50 to 180 GeV where the acceptance is above 10%. The data sample was divided into the three categories:

- events with z in the interval 0.9 to 1;
- events with z in the interval 0.4 to 0.9;
- events with $z < 0.4$.

The first category is interpreted as coming mainly from the diffractive proton dissociation process. The second one is dominated by the photon-gluon process (direct process) and the third is a combination of direct and resolved processes. The $\mu^+\mu^-$ invariant mass for

[1] A cluster is defined as a group of contiguous cells in the CAL with energy above a set threshold.
[2] The pseudorapidity is defined as $\eta = -\ln\tan(\frac{\theta}{2})$.

the second category is shown in Fig. 2a, fitted with a Gaussian plus a flat background giving a mass of 3.086±0.004 GeV. The rms width is 39±4 MeV, consistent with the Monte Carlo expectations. The invariant mass distribution for $z < 0.4$ events is shown in Fig. 2b. Table 1 contains the fitted number of events above background for each category and for various W ranges. The data so collected correspond to events with $Q^2 < 4$ GeV^2. The events selected in the chosen W range have $\sum_i (E_i - p_{Z_i}) < 20$ GeV. Events with the scattered positron in the CAL are expected to have a $\sum_i (E_i - p_{Z_i}) \sim 2E_e = 55$ GeV. A cross check with an electron finder confirmed the absence of large Q^2 events in the sample.

4.2 Electron Mode

Inelastic J/$\psi \to e^+e^-$ candidates were triggered at the FLT by demanding the two conditions:

1. at least one of the following requirements on the CAL energies:
   - CAL total energy > 15 GeV;
   - CAL-EMC energy > 10 GeV;
   - CAL total transverse energy > 11 GeV;
   - BCAL-EMC energy > 3.4 GeV;
   - RCAL-EMC energy > 2.0 GeV;
2. at least one CTD track associated with the nominal vertex.

At the SLT events were rejected if $\sum_i p_{Z_i}/E_{Tot}$ was greater than 0.92 (with p_{Z_i} and E_{Tot} defined as in the previous section). In addition only events satisfying the following two conditions were accepted:

- $\sum_i (E_i - p_{Z_i}) > 4$ GeV, where the sum runs over all calorimeter cells i;
- the sum of the total energy deposits in BCAL-EMC and RCAL-EMC was greater than 3 GeV.

At the TLT a fast electron identification was carried out by using information from the CTD and CAL. Clusters were identified as electrons if at least 90% of the cluster's energy was deposited in the electromagnetic section. The tracks from the CTD were extrapolated towards the CAL and matched to the nearest cluster within 30 cm of the extrapolated track at the CAL face. An event was accepted if at least two oppositely charged tracks, identified as electrons, were found each with a momentum exceeding 0.5 GeV and a transverse momentum greater than 0.4 GeV; in addition, the two tracks were required to originate from points less than 7 cm apart along the Z axis. The invariant mass of the track pair, assuming the electron mass for each track, had to be greater than 2 GeV.

The initial offline selection was based on the TLT track-cluster matching algorithm, but using the full tracking and CAL information.

Since the transverse momentum (p_t) spectrum of the background tracks peaks at low p_t values, both electron track candidates were required to have p_t greater than 0.8 GeV. Also, both tracks had to originate from the event vertex and satisfy the condition $|\eta| < 1.75$. The large background coming mainly from low energy pions faking electrons was further reduced firstly by requiring a tighter matching of the tracks to the electromagnetic clusters, with a track-cluster separation at the CAL face less than 25 cm, secondly by demanding clusters with small longitudinal and radial dimensions and thirdly by imposing a cut $0.4 < E_{cluster}/p < 1.6$, where $E_{cluster}$ is the energy of the electromagnetic cluster and p is the momentum of the associated track. This cut was chosen since, for electrons in the momentum range 1-3 GeV (typical for electrons from J/ψ decays in the present analysis), the inactive material in front of the calorimeter means that the $E_{cluster}/p$ ratio is about 0.8 with 20% resolution.

A significant reduction in the remaining background was achieved by using the RHES and the information on the specific ionisation energy loss, dE/dx, as evaluated from the CTD. The dE/dx of a track, calculated from the truncated mean of a distribution of pulse amplitudes where the lowest 30% and the highest 10% were discarded, had a resolution of about 12%, averaged over a broad range in η ($|\eta| < 1.5$). By requiring dE/dx for one of the electron candidate tracks to be consistent with that expected for an electron, 93% of the e^+e^- pairs were retained, while discarding two thirds of the background[3]. Because the identification of electrons via dE/dx is not well understood for low angle tracks, the use of dE/dx was limited to tracks with $|\eta| < 1$. For $\eta < -1$ the RHES can be used for electron identification. A HES electron cluster was defined as a group of adjacent silicon pads each with an energy deposit above 0.6 m.i.p., and the total energy of all pads above 5 m.i.p. Track-HES cluster matching was then performed for tracks already matched to a CAL cluster, requiring that the distance between the HES cluster and the extrapolated track be less than 10 cm. The efficiency of the cut on the RHES cluster energy above 5 m.i.p. was estimated to be 75% using an almost background-free $J/\psi \to e^+e^-$elastic sample.

Events were then accepted if the electron tracks satisfied one of the following requirements: if both tracks lie in the range $|\eta| < 1$ they had to satisfy the aforementioned dE/dx cut; if one track was in the range $|\eta| < 1$ and the other in $\eta < -1$ they had to satisfy the dE/dx and the RHES cuts, respectively. All the other track combinations were not considered due to the presence of high background.

The final inelastic data sample was defined by requiring an energy deposit greater than 1 GeV in a cone of 35^o around the forward direction (excluding the calorimeter deposits due to the electrons). A minimum value of z was required ($z > 0.5$) to avoid the low z region which is dominated by large background. The data were also restricted to the W range 90 to 180 GeV, where the acceptance is high. Using the z variable the electron data sample was divided in two categories: $z > 0.9$ and $0.5 < z < 0.9$.

[3]The 93% efficiency was computed from γ conversions and almost background-free $J/\psi \to e^+e^-$elastic events.

Figure 2c shows the mass distribution of the electron pairs for the second category. A clear peak at the J/ψ mass is observed. The solid line shows an unbinned likelihood fit in which a Gaussian resolution function has been convoluted with a radiative J/ψ mass spectrum and a linear distribution to describe the background (dashed line). The mass estimated by the fit is 3.089 ± 0.010 GeV. The rms width is 40 ± 9 MeV, consistent with the MC expectation. Table 1 contains, for the two categories and W ranges, the fitted number of events above background. As for the muon sample, the data so collected correspond to events with $Q^2 < 4$ GeV^2.

5 Monte Carlo Simulation and Acceptance Calculation

Inelastic J/ψ production from direct photon-gluon fusion was simulated using the colour-singlet model as implemented in the HERWIG [24] parton shower generator. The range of Q^2 was from the kinematic limit ($\approx 10^{-10}$ GeV^2) to 4 GeV^2. The energy scale, μ^2, at which the gluon distribution is evaluated was chosen to be $\mu^2 = 2\hat{s}\hat{t}\hat{u}/(\hat{s}^2+\hat{t}^2+\hat{u}^2)$, where $\hat{s}$, $\hat{t}$ and $\hat{u}$ are the Mandelstam variables of the photon-gluon fusion process. The mean value of μ^2 is 7 GeV^2. The gluon structure function in the proton was parameterized with the MRSD$'_-$ [25] distribution.

For resolved J/ψ production the PYTHIA [26] parton shower generator was used with the GRV proton [27] and photon [28] parton densities. The matrix elements for resolved photon processes were computed in the colour-singlet framework.

Production of J/ψ mesons accompanied by diffractive proton dissociation was simulated with EPSOFT [29]. This generator is based on the assumption that the diffractive cross section is of the form $d\sigma/d|t|dM_N^2 \propto e^{-b_d|t|}/M_N^\beta$, where M_N is the mass of the dissociative system, and t is the four-momentum transfer squared at the proton vertex. The value of b_d was chosen to be 1 GeV^{-2} to reproduce the observed p_T^2 distribution of events with $z > 0.9$. For the M_N distribution, the value $\beta = 2$ was used. The simulation of the dissociative system includes a parametrisation of the resonance spectrum.

In the muon case a mixture of HERWIG $(78^{+4}_{-6})\%$ and EPSOFT events gives the best description of the z distribution with z ranging from 0.4 to 1. For the electron case the percentage is $(79\pm6)\%$. The same mixture also describes well all the reconstructed kinematic variables (see Fig. 3 for some examples). The resolution in z is 2% at $z = 0.9$ and increases to 12% at $z = 0.4$. The measured values of z suffer from a systematic shift due to the energy loss in the inactive material in front of the calorimeter and to the undetected particles escaping in the beampipe. This shift is 20% at $z = 0.4$ and becomes negligible at $z = 0.9$. The shift of z was corrected using the HERWIG Monte Carlo.

The acceptance was estimated as the ratio of the number of accepted Monte Carlo photon-gluon fusion events to the number generated in the selected kinematic range. The acceptance, calculated in this manner, accounts for the geometric acceptance, for the detector, trigger and reconstruction efficiencies, and for the detector resolution. Table 2 reports the acceptances in various W ranges determined for each decay mode.

6 Backgrounds to the photon-gluon fusion process

In this section we discuss all the resonant processes which are backgrounds to the photon-gluon fusion process. To calculate integrated and differential cross sections the analysis was restricted to the region $0.4 < z < 0.9$ and $50 < W < 180$ GeV for the muon mode, and to the region $0.5 < z < 0.9$ and $90 < W < 180$ GeV for the electron mode. The upper z cut is necessary to exclude diffractive J/ψ production; the lower cut restricts the data to a range with low background and where the photon-gluon process is expected to dominate over the resolved production. Table 1 reports the numbers of events coming from the fit to the J/ψ mass peak, divided into four W intervals for the muon mode and three intervals for the electron mode. These numbers include proton diffractive dissociation events which migrated from the region above $z = 0.9$. The background from diffractive events was estimated to be $f^{diff} = (8 \pm 2)\%$ in the muon mode and $f^{diff} = (4 \pm 1)\%$ in the electron mode using EPSOFT and following the method explained in section 5. The cross sections were corrected for the estimated fraction of proton dissociative events. The difference in the size of the contamination between muon and electron decay mode reflects the different W range covered.

At the lower end of the z range one has to consider resolved J/ψ photoproduction events for $z > 0.4(0.5)$ as well as migration of resolved events from $z < 0.4$ (0.5) into the region studied. In Fig. 2b the invariant mass plot of the muon decay mode for events with $z < 0.4$ and $50 < W < 180$ GeV is shown. The estimated number of J/ψ events is 19 ± 6. As determined from the z shape of resolved and direct photon Monte Carlo generated events, about 50% of the detected events can be attributed to resolved photoproduction. Their contribution in the $0.4 < z < 0.9$ range, after diffractive proton dissociation subtraction, is $3^{+3}_{-2}\%$. This background has been subtracted from the signal events assuming the W and z dependence given by PYTHIA Monte Carlo. Due to the small statistics of the electron sample the muon result was also used in the electron case.

Production of ψ' mesons with subsequent decay into J/ψ is a contribution not included in the simulation. It is estimated in [1], through phase space considerations, to be 15% of the J/ψ integrated cross section. This result is in good agreement with estimations made by using the value of the ψ' to J/ψ ratio coming from low energy data [9, 10]. This contribution was not subtracted.

7 Systematic Errors

Several factors contribute to the systematic errors in the inelastic J/ψ cross section measurement. In the following they are divided in two categories: *decay channel specific errors* and *common systematic errors*. The first category contains systematic errors specific to the electron or muon decay channel, while the second contains systematic errors common to both decay modes.

Decay channel specific errors:

- *Trigger*: for the muon mode the principal source of uncertainty is the FLT calorimeter trigger. The corresponding error was estimated by using independent muon triggers, which use different calorimeter trigger logic or do not use the calorimeter at all. Also for the electron mode the uncertainty is dominated by the FLT calorimeter simulation and the corresponding error was estimated by using independent calorimeter triggers. The size of the error depends on the W range and is of the order of $\pm 4\%$ in the lowest W bin and of $\pm 1\%$ in the highest one.

- *Event selection*: this class comprises the systematic errors due to the uncertainties in the measurement of momentum, transverse momentum and η of the leptonic tracks. For the muon channel this class contains also the uncertainties coming from the $p_{t1} + p_{t2} > 2.8$ GeV cut and the collinearity cut. For the electron channel uncertainties in the definition of an electron cluster also contribute. Each cut was varied within a range determined by the resolution of the variable to which the cut is applied and the different contributions obtained were summed in quadrature. This error amounts to $\pm 2\%$, almost independent of W.

- *Muon chamber efficiency*: the systematic error ($\pm 2\%$) attributed to uncertainties in the muon chamber reconstruction efficiency was estimated using cosmic ray events.

- *dE/dx*: the error takes into account the uncertainty of the variation in the efficiency of the $\mathrm{d}E/\mathrm{d}x$ cut as a function of the track's polar angle, not reproduced by the Monte Carlo simulation. The size of the error depends on the W range and is of the order of $\pm 7\%$ in the lowest W bin and of $\pm 5\%$ in the highest one.

- *RHES*: the error ($+1\%$) was estimated by rising the cut value from 5 m.i.p. to 6 m.i.p. in the Monte Carlo simulation only. This was done to take into account possible differences of the calibration in the simulation and in the data.

- *Fitting procedure*: different fitting procedures for the J/ψ mass peak were applied to the electron channel and the results were the same within the statistical uncertainty. The size of the error is –3%.

- *Branching Ratio*: the error on the branching ratio $\mathrm{J}/\psi \to l^+l^-$ is used as quoted in [32] ($\pm 3.2\%$).

Common systematic errors:

- *Parton density*: the uncertainty in the acceptance resulting from the uncertainty in the form of the gluon distribution was estimated by changing the default gluon distribution (MRSD$^{'}_{-}$ [25]) with others (GRV [27], MRSG [30], MRSA$^{'}$ [30]). This error is of the order of $\pm 1\%$ in all the W ranges, except in the highest W bin where it contributes –8%.

- *Energy scale*: the calorimeter energy scale in the Monte Carlo was varied by $\pm 5\%$. This affects mainly the W and z determinations and gives a $\pm 2\%$ contribution.

- *Proton dissociation*: The parameters β and b_d were varied from $\beta = 2$ to $\beta = 2.5$ ($\beta = 2.20 \pm 0.03$ is the result of [31]) and from $b_d = 0.9$ GeV^{-2} to $b_d = 1.3$ GeV^{-2} (from the analysis of the p_T^2 distribution of the events with $z > 0.9$). This systematic uncertainty is dominated by the number of events with $z > 0.9$ and is concentrated in the range $50 < W < 90$ GeV, where it gives a contribution of $\pm 5\%$, while in the other bins it is of the order of the $\pm 1\%$ or lower.

- *Resolved photon*: this systematic error contains contributions from the limited statistics of the muon sample for $z < 0.4$ and the uncertainties in the Monte Carlo modelling of the resolved process. The corresponding error was evaluated to be $\pm 4\%$, independent from W.

- *z extrapolation*: the cross sections were measured down to $z = 0.4$ for the muon channel and to $z = 0.5$ for the electron channel and then extrapolated to zero using the HERWIG Monte Carlo. The uncertainty ($\pm 3.5\%$) on the extrapolation was evaluated by varying Λ_{QCD} and the charm mass, m_c, in the NLO calculation.

- *Angular distribution*: The angular distribution of the decay leptons was modelled using the form $(1 + \alpha \cos^2 \theta^*)$, where θ^* is the decay angle of the leptons in the J/ψ rest frame with respect to the direction of the J/ψ momentum in the laboratory. The data are best described with $\alpha = 0$, that is a flat distribution. As a systematic check α was varied by one standard deviation (i.e. up to $\alpha = 0.5$); this gave an error growing from $+5\%$ in the lowest W bin to $+8\%$ in the highest W bin.

- *Luminosity*: as indicated in section 2.2, the uncertainty on the luminosity determination is $\pm 1.5\%$.

The total systematic error, given by the sum in quadrature of all the common and uncommon systematic errors, is of the order of $\pm 10\%$ ($\pm 15\%$) for the muon (electron) decay channel.

8 Results

8.1 Cross Section Calculation

The electroproduction cross section for inelastic J/ψ production, after subtracting the contributions of diffractive proton dissociation and of resolved photon processes, is calculated as:

$$\sigma(e^+ p \to e^+ \mathrm{J}/\psi X) = \frac{N_{evt}}{\mathcal{A}\,\mathcal{L}\,\mathcal{B}}, \tag{5}$$

where N_{evt} denotes the background subtracted number of J/ψ signal events, $\mathcal{A}$ the acceptance, $\mathcal{L}$ the integrated luminosity and $\mathcal{B}$ the J/ψ leptonic branching fraction [32], namely $(6.01 \pm 0.19)\%$ for $\mu^+\mu^-$ and $(6.02 \pm 0.19)\%$ for e^+e^-. The photoproduction cross section is related to the ep cross section by [33]

$$\sigma_{\gamma p \to J/\psi X} = \frac{\int_{y_{min}}^{y_{max}} \int_{Q^2_{min}(y)}^{Q^2_{max}} \Phi(y, Q^2) \sigma_{\gamma p \to J/\psi X}(y, Q^2) dy dQ^2}{\Phi_T} = \frac{\sigma_{e^+ p \to e^+ J/\psi X}}{\Phi_T}, \tag{6}$$

where $\sigma_{\gamma p \to J/\psi X}$ is the mean cross section in the measured range of W (corresponding to the limits y_{min}, y_{max}) and Q^2. The effective flux, Φ_T, of virtual photons from the positron is computed as:

$$\Phi_T = \int_{y_{min}}^{y_{max}} \int_{Q^2_{min}(y)}^{Q^2_{max}} \Phi(y, Q^2) dy dQ^2 = \int_{y_{min}}^{y_{max}} \int_{Q^2_{min}(y)}^{Q^2_{max}} \frac{\alpha}{2\pi y Q^2}[1 + (1-y)^2 - \frac{2M_e^2 y^2}{Q^2}] dy dQ^2, \quad (7)$$

where α is the electromagnetic coupling constant. The integrals run from $Q^2_{min} = M_e^2 \frac{y^2}{1-y}$ to $Q^2_{max} = 4$ GeV^2 and from $y_{min} = W^2_{min}/s$ to $y_{max} = W^2_{max}/s$ where W_{min} and W_{max} are the minimum and maximum values of W, respectively, in each chosen interval.

The electro- and photoproduction cross sections are summarized in Tab. 2 for the two J/ψ decay channels. The first error is statistical and the second comes from adding in quadrature all the systematic errors described in section 7. The cross sections measured in the restricted z ranges were extrapolated to $z = 0$ (using HERWIG) in order to be able to compare with other available data. The size of the extrapolation ($\sim 10\%$ for the muon decay mode and $\sim 25\%$ for the electron decay mode) and the associated systematic error are shown in Tab. 2 and given in section 7. The difference in the size of the extrapolation between muon and electron decay modes is due to the different z ranges measured. Table 3 reports for the lowest W bin the photoproduction cross section from the muon channel only and for the following three W bins the combined muon and electron photoproduction cross sections. These results are given both in the range $0.4 < z < 0.9$ and in the extrapolated range $z < 0.9$. To obtain the combined results a weighted mean was calculated; the weights were obtained by summing the statistical and decay channel specific errors in quadrature. The first error for the combined results in Tab. 3 is the error on the weighted mean, the second is given by the sum of the common systematic errors added in quadrature. The photoproduction cross sections for $z < 0.9$ are shown in Fig. 4 together with those found by the H1 collaboration [15] and a compilation of fixed target results [9, 10, 14]. The ZEUS and H1 data are compatible. The cross section rises as W increases. The curves in the plot correspond to the NLO calculation [1] computed with no cut on the p_T of the J/ψ , $z < 0.9$, with a charm mass (m_c) of 1.4 GeV, $\Lambda_{QCD} = 300$ MeV and with renormalization and factorization scales of $\sqrt{2}m_c$. Dashed, continuous and dashed-dotted curves are obtained with different gluon distributions (MRSG [30], GRV [27] and CTEQ3M [34], respectively), compatible with those extracted from F_2 measurements at HERA [35, 36]. The theoretical predictions were multiplied by a factor 1.15 to take into account ψ' production. The predictions are in qualitative agreement with the data, but the distinction among different parton densities is not possible because the NLO calculation is not well behaved in the limit $p_T \to 0$. Furthermore, there is a significant dependence on the values of the charm mass and Λ_{QCD}. The cross section varies as $1/m_c^3$ and α_s^2 as illustrated by the dotted line which is calculated with $m_c = 1.55$ GeV and $\Lambda_{QCD} = 215$ MeV and using the GRV gluon distribution.

A more quantitative comparison between data and theory can be made in the restricted kinematic range $p_T^2 > 1$ GeV^2, where the calculation is much more reliable. The NLO computation now allows an absolute comparison between data and models. The cross sections for this kinematic range are summarized in Tab. 2 for the two J/ψ decay channels and in Tab. 3 for the combined result, with the additional requirement $z < 0.8$ in order to compare with [15]. The measured cross sections for $z < 0.8$ and $p_T^2 > 1$ GeV^2 are

displayed in Figure 5. The curves represent the NLO calculation using the different gluon distributions cited above. Data and theory are in good agreement using $m_c = 1.4$ GeV, $\Lambda_{QCD} = 300$ MeV and $\sqrt{2}m_c$ as renormalization factor. While for $z < 0.9$ and all p_T^2 the predictions are significantly different for different parametrizations of the gluon density, this is not so in the more restricted domain $z < 0.8$ and $p_T^2 > 1$ GeV^2. This is a consequence of the p_T^2 cut: the gluon distribution is probed at larger x_g values, where the differences between the various gluon densities are smaller; here x_g is the proton energy fraction carried by the incoming gluon. In the present analysis, with $z < 0.9$ we explore the range $4 \cdot 10^{-4} \lesssim x_g \lesssim 10^{-2}$, and the range $10^{-3} \lesssim x_g \lesssim 10^{-2}$ in the restricted interval.

8.2 Transverse Momentum Distribution

Figure 6 shows the differential cross section $\mathrm{d}\sigma/\mathrm{d}p_T^2$ for $z < 0.9$ and $50 < W < 180$ GeV using only the muon sample. The background contributions listed in section 6 were subtracted bin by bin. The curve shows the NLO prediction obtained with $m_c = 1.4$ GeV, $\Lambda_{QCD} = 300$ MeV, $\sqrt{2}m_c$ as scale and GRV for the gluon distribution[4]. For $p_T^2 > 1$ GeV^2 data and theoretical calculation are in good agreement. A fit of the function

$$\frac{d\sigma}{dp_T^2} = Ae^{-bp_T^2} \tag{8}$$

to our data was performed in the range $1 < p_T^2 < 9$ GeV^2 giving

$$b = 0.32 \pm 0.03\ (\mathrm{stat}) \pm 0.01(\mathrm{syst})\ \mathrm{GeV}^{-2}. \tag{9}$$

A similar fit to the NLO calculation [1] yields a slope of $b = 0.3$ GeV^{-2} above $p_T^2 > 1$ GeV^2. The systematic error contains contributions from all the classes of systematic errors discussed in section 7 and also from the change in the p_T^2 fitting interval.

8.3 Distribution of z

Figure 7 shows the differential cross section $\mathrm{d}\sigma/\mathrm{d}z$ for $p_T^2 > 1$ GeV^2 and $50 < W < 180$ GeV as obtained using only the muon sample. It is compared to the NLO calculation [1] discussed in section 8.1 and with the parameters used in 8.2. Agreement in shape and normalization is found within the errors. Our data are in good agreement with the result of the H1 collaboration [15].

Recently there has been theoretical activity attempting to solve the discrepancy between the J/ψ production cross section measurements in hadronic reactions and the colour-singlet model by invoking additional octet contributions [37]. A specific leading order calculation of J/ψ photoproduction at HERA has been carried out using values of the nonperturbative colour-octet terms determined from a fit [8] to the CDF data [6]. These calculations predict a cross section for HERA rising with z, which is not seen in the data. This is illustrated in Fig.7 where the dashed line shows a sum of the colour-singlet and colour-octet contributions both calculated at leading order.

[4]The NLO p_T^2 and z distributions for the ψ' have large theoretical uncertainties and cannot be accounted for simply by a scale factor.

9 Conclusion

We have measured inelastic J/ψ photoproduction in the range $50 < W < 180$ GeV and $0.4 < z < 0.9$. The cross section rises with W. In this z interval the photon-gluon fusion process is expected to dominate. A NLO calculation for the photon-gluon fusion process agrees with the data both for the integrated cross section and the differential distributions over z and p_T^2 in the kinematic range $z < 0.8$ and $p_T^2 > 1$ GeV^2, using gluon distribution parametrizations compatible with those determined from the F_2 measurements performed at HERA. The predictions of a specific leading order colour-octet model, as formulated to fit the CDF data on J/ψ hadroproduction, are not consistent with the data.

Acknowledgements

We thank the DESY Directorate for their strong support and encouragement. The remarkable achievements of the HERA machine group were essential for the successful completion of this work and are gratefully acknowledged. We are also grateful to M. Cacciari, M. Krämer, and P. A. Zerwas for providing the theoretical curves and for many useful discussions.

References

[1] M. Krämer et al., Phys. Lett. B348 (1995) 657;
M. Krämer, Nucl. Phys. B459 (1996) 3.

[2] E.L. Berger and D. Jones, Phys. Rev. D23 (1981) 1521.

[3] M. Krämer, private communication.

[4] H. Jung, G.A. Schuler and J. Terron, Int. Jour. of Mod. Phys. A7 (1992) 7955.

[5] R. Baier and R. Rückl, Phys. Lett. B102 (1981) 364.

[6] CDF Collab., F. Abe et al., Phys. Rev. Lett. 69 (1992) 3704;
CDF Collab., A. Sansoni, FERMILAB-CONF-95/263-E.

[7] G.T. Bodwin, E. Braaten and G.P. Lepage, Phys. Rev. D51 (1995) 1125.

[8] M. Cacciari and M. Krämer, Phys. Rev. Lett. 76 (1996) 4128.

[9] FTPS Collab., B.H. Denby et al., Phys. Rev. Lett. 52 (1984) 795.

[10] NA14 Collab., R. Barate et al., Z. Phys. C33 (1987) 505.

[11] BFP Collab., A.R. Clark et al., Phys. Rev. Lett. 43 (1979) 187.

[12] EMC Collab., J.J. Aubert et al., Nucl. Phys. B213 (1983) 1.

[13] NMC Collab., D. Allasia et al., Phys. Lett. B258 (1991) 493.

[14] EMC Collab., J. Ashman et al., Z. Phys. C56 (1992) 21.

[15] H1 Collab., S. Aid et al., Nucl. Phys. B472 (1996) 3.

[16] ZEUS Collab., The ZEUS Detector, Status Report, DESY (1993).

[17] C. Alvisi et al., Nucl. Instr. Meth. A305 (1991) 30.

[18] N. Harnew et al., Nucl. Instr. Meth. A279 (1989) 290;
C.B. Brooks et al., Nucl. Instr. Meth. A283 (1989) 477;
B. Foster et al., Nucl. Instr. Meth. A338 (1994) 254.

[19] M. Derrick et al., Nucl. Instr. Meth. A309 (1991) 77;
A. Andresen et al., Nucl. Instr. Meth. A309 (1991) 101;
A. Bernstein et al., Nucl. Instr. Meth. A336 (1993) 23.

[20] A. Dwurazny et al., Nucl. Instr. Meth. A277 (1989) 176;
ZEUS Collab., M. Derrick et al., Z. Phys. C73 (1996) 73.

[21] G. Abbiendi et al., Nucl. Instr. Meth. A333 (1993) 342.

[22] D. Kisielewska et al., DESY-HERA 85-25 (1985);
J. Andruszków et al., DESY-92-066 (1992).

[23] F. Jacquet and A. Blondel, in Proceedings of the study for an ep facility in Europe 79/48 (1979) 391.

[24] G. Marchesini et al., Comp. Phys. Com. 67 (1992) 465;
B.R. Webber, DESY 92–028, Proc. of the Workshop 'Physics at HERA', Vol III., Oct 1991, p. 1354;
L. Stanco, ibidem, p. 1363.

[25] A. D. Martin, W. J. Stirling and R. G. Roberts, Phys. Lett. B306 (1993) 145.

[26] T. Sjöstrand and M. Bengtsson, Comp. Phys. Comm. 43 (1987) 367;
M. Bengtsson and T. Sjöstrand, Comp. Phys. Comm. 46 (1987) 43;
T. Sjöstrand, Proc. of the Workshop 'Physics at HERA', Vol. III, Oct. 1991, 1405.

[27] M. Glück, E. Reya and A. Vogt, Z. Phys. C53 (1992) 127;
M. Glück, E. Reya and A. Vogt, Z. Phys. C53 (1992) 651.

[28] M. Glück, E. Reya and A. Vogt, Phys. Rev. D46 (1992) 1973.

[29] M. Kasprzak, PhD Thesis, Warsaw University, DESY-Internal Report F35D-96-16 (1996).

[30] A. D. Martin, W. J. Stirling and R. G. Roberts, Phys. Lett. B354 (1995) 155.

[31] CDF Collab., F. Abe et al., Phys. Rev. D50 (1994) 5535.

[32] Particle Data Group, R.M. Barnett et al., Phys. Rev. D54 (1996) 1.

[33] V.N. Gribov et al., Sov. Phys. JETP 14 (1962) 1308;
V.M. Budnev et al., Phys. Rep. C15 (1975) 181.

[34] H.L. Lai et al., Phys. Rev. D51 (1995) 4763.

[35] ZEUS Collab., M. Derrick et al., Phys. Lett. B316 (1993) 412;
ZEUS Collab., M. Derrick et al., Z. Phys. C65 (1995) 379;
ZEUS Collab., M. Derrick et al., Z. Phys. C69 (1996) 607;
ZEUS Collab., M. Derrick et al., Z. Phys. C72 (1996) 399.

[36] H1 Collab., I. Abt et al., Nucl. Phys. B407 (1993) 515;
H1 Collab., T. Ahmed et al., Nucl. Phys. B439 (1995) 471;
H1 Collab., S. Aid et al., Nucl. Phys. B470 (1996) 3;
H1 Collab., C. Adloff et al., DESY 97-042.

[37] E. Braaten and S. Fleming, Phys. Rev. Lett. 74 (1995) 3327;
P. Cho and A.K. Leibovich, Phys. Rev. D53 (1996) 6203;
B. Cano-Coloma and M.A. Sanchis-Lozano, IFIC/97-29, hep-ph/9706270.

$J/\psi \to \mu^+\mu^-$				
W range (GeV)	50-90	90-120	120-150	150-180
$0.9 < z < 1$	14±4	29±6	27±6	12±5
$0.4 < z < 0.9$	67±9	53±8	35±7	26±7
$z < 0.4$	19±6			
$J/\psi \to e^+e^-$				
W range (GeV)	50-90	90-120	120-150	150-180
$0.9 < z < 1$		22 ± 6		
$0.5 < z < 0.9$		20±6	33±7	7±3

Table 1: Number of events in the various z and W ranges for $J/\psi \to \mu^+\mu^-$ and e^+e^-.

$J/\psi \to \mu^+\mu^-$, $z < 0.9$						
W (GeV)	$< W >$ (GeV)	$\mathcal{A}$	$\sigma_{ep}(0.4< z <0.9)$ (nb)	$\sigma_{ep}(z <0.9)$ (nb)	Φ_T	$\sigma_{\gamma p}(z <0.9)$ (nb)
50-90	73	18%	$1.74\pm0.23^{+0.19}_{-0.14}$	$1.92\pm0.25^{+0.22}_{-0.17}$	0.0555	$34.6\pm4.5^{+4.0}_{-3.1}$
90-120	105	24%	$1.10\pm0.17^{+0.10}_{-0.07}$	$1.23\pm0.19^{+0.12}_{-0.09}$	0.0232	$53.0\pm8.2^{+5.2}_{-4.0}$
120-150	134	24%	$0.75\pm0.14^{+0.08}_{-0.04}$	$0.84\pm0.16^{+0.09}_{-0.06}$	0.0157	$53.5\pm10.2^{+5.7}_{-3.8}$
150-180	162	16%	$0.81\pm0.20^{+0.08}_{-0.07}$	$0.90\pm0.22^{+0.10}_{-0.09}$	0.0110	$81.8\pm20.0^{+9.1}_{-8.2}$
$J/\psi \to e^+e^-$, $z < 0.9$						
W (GeV)	$< W >$ (GeV)	$\mathcal{A}$	$\sigma_{ep}(0.5< z <0.9)$ (nb)	$\sigma_{ep}(z <0.9)$ (nb)	Φ_T	$\sigma_{\gamma p}(z <0.9)$ (nb)
90-120	107	16%	$0.63\pm0.20^{+0.10}_{-0.06}$	$0.79\pm0.25^{+0.14}_{-0.08}$	0.0232	$34.1\pm10.8^{+6.0}_{-3.4}$
120-150	136	20%	$0.85\pm0.18^{+0.10}_{-0.09}$	$1.05\pm0.22^{+0.13}_{-0.13}$	0.0157	$66.9\pm14.0^{+8.3}_{-8.3}$
150-180	166	7%	$0.55\pm0.25^{+0.07}_{-0.09}$	$0.68\pm0.31^{+0.09}_{-0.11}$	0.0110	$61.8\pm28.2^{+8.2}_{-10.0}$
$J/\psi \to \mu^+\mu^-$, $z < 0.8$, $p_T^2 > 1$ GeV^2						
W (GeV)	$< W >$ (GeV)	$\mathcal{A}$	$\sigma_{ep}(0.4< z <0.8)$ (nb)	$\sigma_{ep}(z <0.8)$ (nb)	Φ_T	$\sigma_{\gamma p}(z <0.8)$ (nb)
50-80	70	16%	$0.80\pm0.18^{+0.09}_{-0.05}$	$0.93\pm0.21^{+0.11}_{-0.06}$	0.0452	$20.6\pm4.6^{+2.5}_{-1.4}$
80-110	96	22%	$0.65\pm0.12^{+0.07}_{-0.05}$	$0.76\pm0.14^{+0.09}_{-0.07}$	0.0268	$28.4\pm5.2^{+3.2}_{-2.5}$
110-180	138	18%	$0.89\pm0.19^{+0.09}_{-0.08}$	$1.04\pm0.22^{+0.12}_{-0.10}$	0.0334	$31.1\pm6.6^{+3.5}_{-3.1}$
$J/\psi \to e^+e^-$, $z < 0.8$, $p_T^2 > 1$ GeV^2						
W (GeV)	$< W >$ (GeV)	$\mathcal{A}$	$\sigma_{ep}(0.5< z <0.8)$ (nb)	$\sigma_{ep}(z <0.8)$ (nb)	Φ_T	$\sigma_{\gamma p}(z <0.8)$ (nb)
110-180	142	15%	$0.70\pm0.18^{+0.08}_{-0.09}$	$0.96\pm0.25^{+0.12}_{-0.13}$	0.0334	$28.7\pm7.5^{+3.6}_{-3.9}$

Table 2: Inelastic J/ψ photoproduction cross sections for the muon and electron decay modes in the two regions $z < 0.9$ and $z < 0.8$, $p_T^2 > 1$ GeV^2. From left to right we give the W range, the W mean value ($< W >$), the acceptance ($\mathcal{A}$), the measured ep cross sections, the ep cross sections extrapolated to $z = 0$, the flux factor (Φ_T) and finally the γp cross sections.

W (GeV)	$< W >$ (GeV)	$\sigma_{\gamma p}$ $(0.4 < z < 0.9)$ (nb)	$\sigma_{\gamma p}$ $(z < 0.9)$ (nb)
50-90	73	$31.4 \pm 4.1^{+3.4}_{-2.5}$	$34.6 \pm 4.5^{+4.0}_{-3.1}$
90-120	106	$41.4 \pm 6.0^{+3.0}_{-1.3}$	$46.1 \pm 7.0^{+3.6}_{-2.2}$
120-150	135	$51.0 \pm 7.6^{+4.5}_{-1.9}$	$57.8 \pm 8.7^{+5.6}_{-3.0}$
150-180	162	$68.2 \pm 14.5^{+6.4}_{-5.5}$	$75.3 \pm 16.6^{+7.4}_{-6.9}$
W (GeV)	$< W >$ (GeV)	$\sigma_{\gamma p}$ $(0.4 < z < 0.8, p_T^2 > 1$ GeV$^2)$ (nb)	$\sigma_{\gamma p}$ $(z < 0.8, p_T^2 > 1$ GeV$^2)$ (nb)
50-80	70	$17.7 \pm 4.0^{+2.0}_{-1.1}$	$20.6 \pm 4.6^{+2.5}_{-1.4}$
80-110	96	$24.3 \pm 4.5^{+2.6}_{-1.9}$	$28.4 \pm 5.2^{+3.2}_{-2.5}$
110-180	140	$25.7 \pm 4.2^{+2.4}_{-2.1}$	$30.1 \pm 5.2^{+3.0}_{-2.7}$

Table 3: Cross sections $\sigma_{\gamma p \to J/\psi X}$ for the phase space regions: $0.4 < z < 0.9$ (top-left), $z < 0.9$ (top-right), $0.4 < z < 0.8$ and $p_T^2 > 1$ GeV^2 (bottom-left), $z < 0.8$ and $p_T^2 > 1$ GeV^2 (bottom-right). The cross sections for $0.4 < z < 0.9$ and for $z < 0.9$ in the W range from 50 to 90 GeV come from the muon channel only. The first error is statistical, the second one comes from all the systematic errors added in quadrature. The other three measurements come from the combination of the electron and muon results as described in the text. The first error contains the contribution from statistical and decay channel specific errors while the second contains all sources of common systematic errors. In the regions $0.4 < z < 0.8$, $p_T^2 > 1$ GeV^2 and $z < 0.8$, $p_T^2 > 1$ GeV^2 for W in the range from 50 to 110 GeV only the muon channel data are used while for the highest bin electron and muon results were combined as explained in the text.

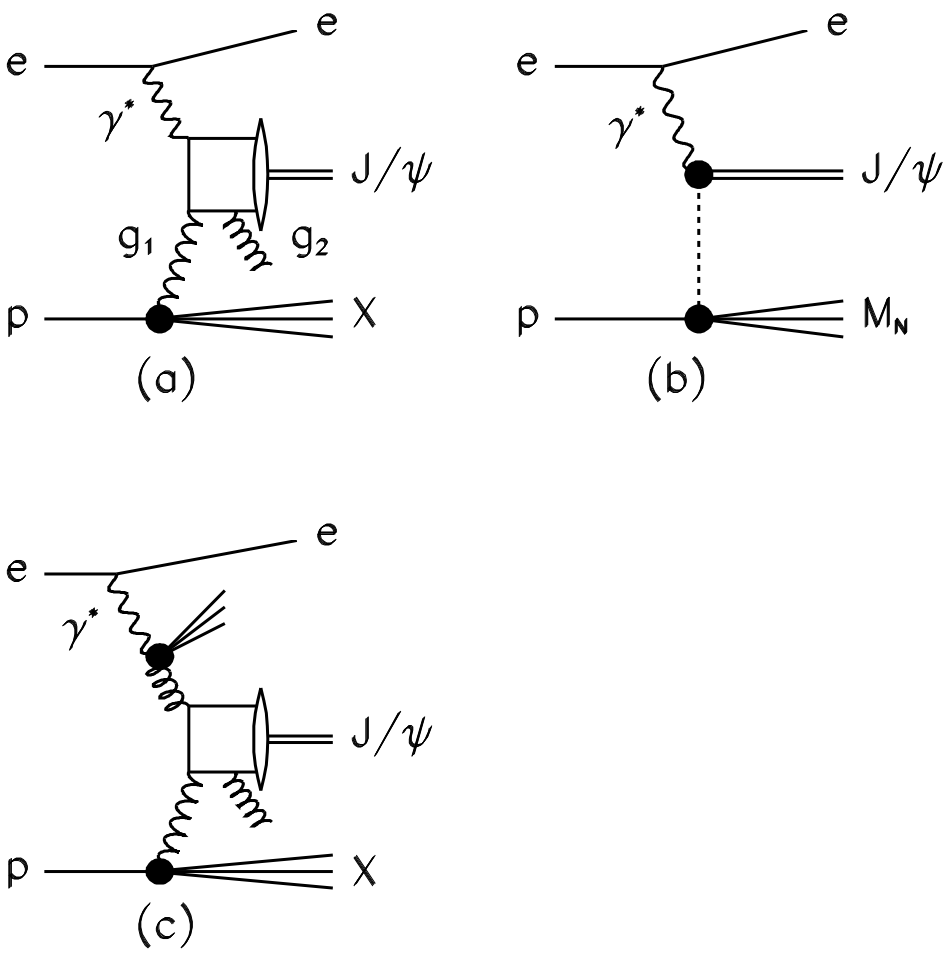

Figure 1: Dominant inelastic J/ψ production mechanisms at HERA. Photon-gluon fusion is described by diagram (a). Diagrams (b) and (c) correspond to diffractive proton dissociation and resolved photon J/ψ production, respectively.

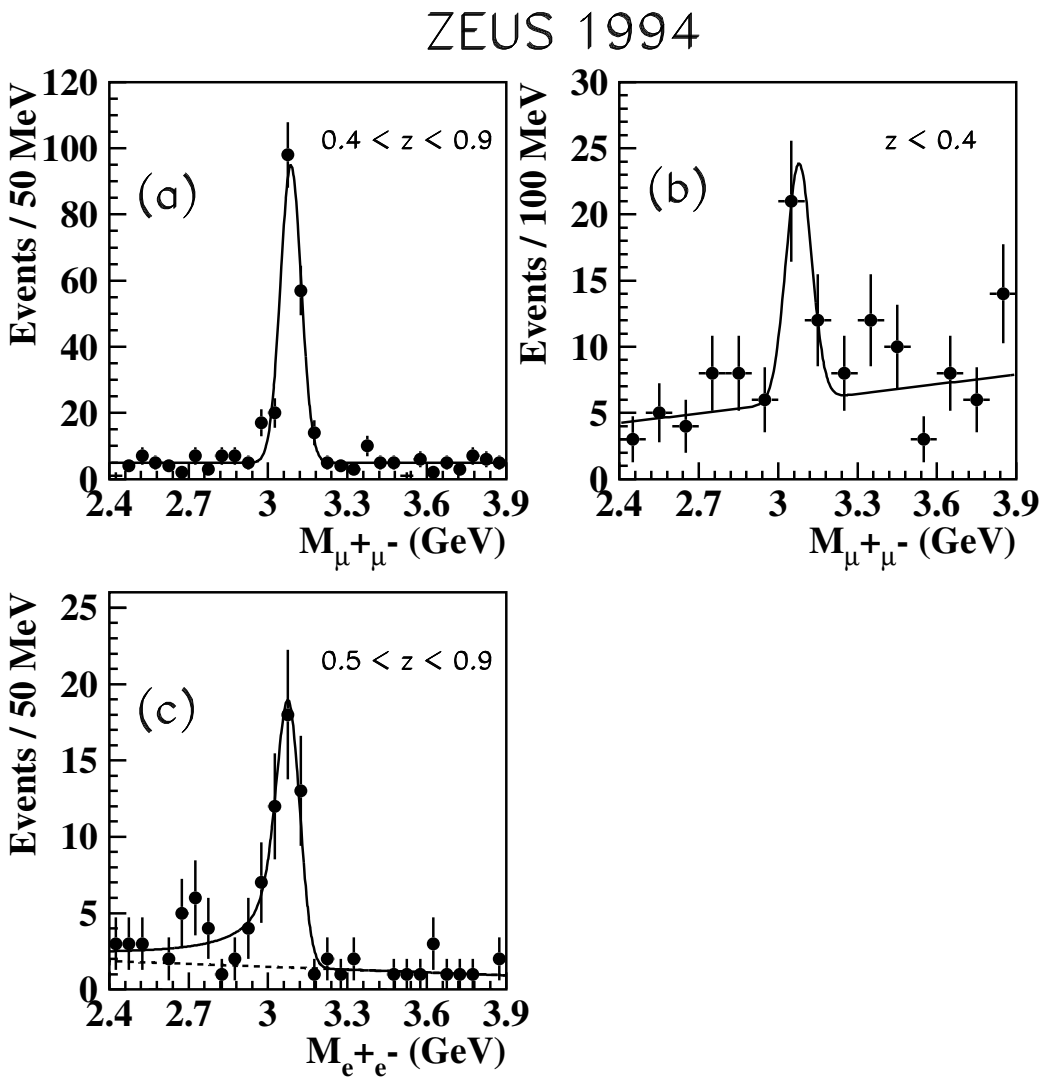

Figure 2: Invariant mass spectrum for the muon pair sample (a) for $0.4 < z < 0.9$ and (b) for $z < 0.4$, in the W range 50 to 180 GeV. The invariant mass spectrum for the electron pair sample ($0.5 < z < 0.9$ and $90 < W < 180$ GeV) is shown in (c). The muon mass spectrum (a) was fitted to the sum of a Gaussian and a flat background; the spectrum (b) was fitted to the sum of a Gaussian and a linear background. The electron mass spectrum (c) was fitted to the sum of the convolution of a Gaussian and a bremsstrahlung function plus a linear background.

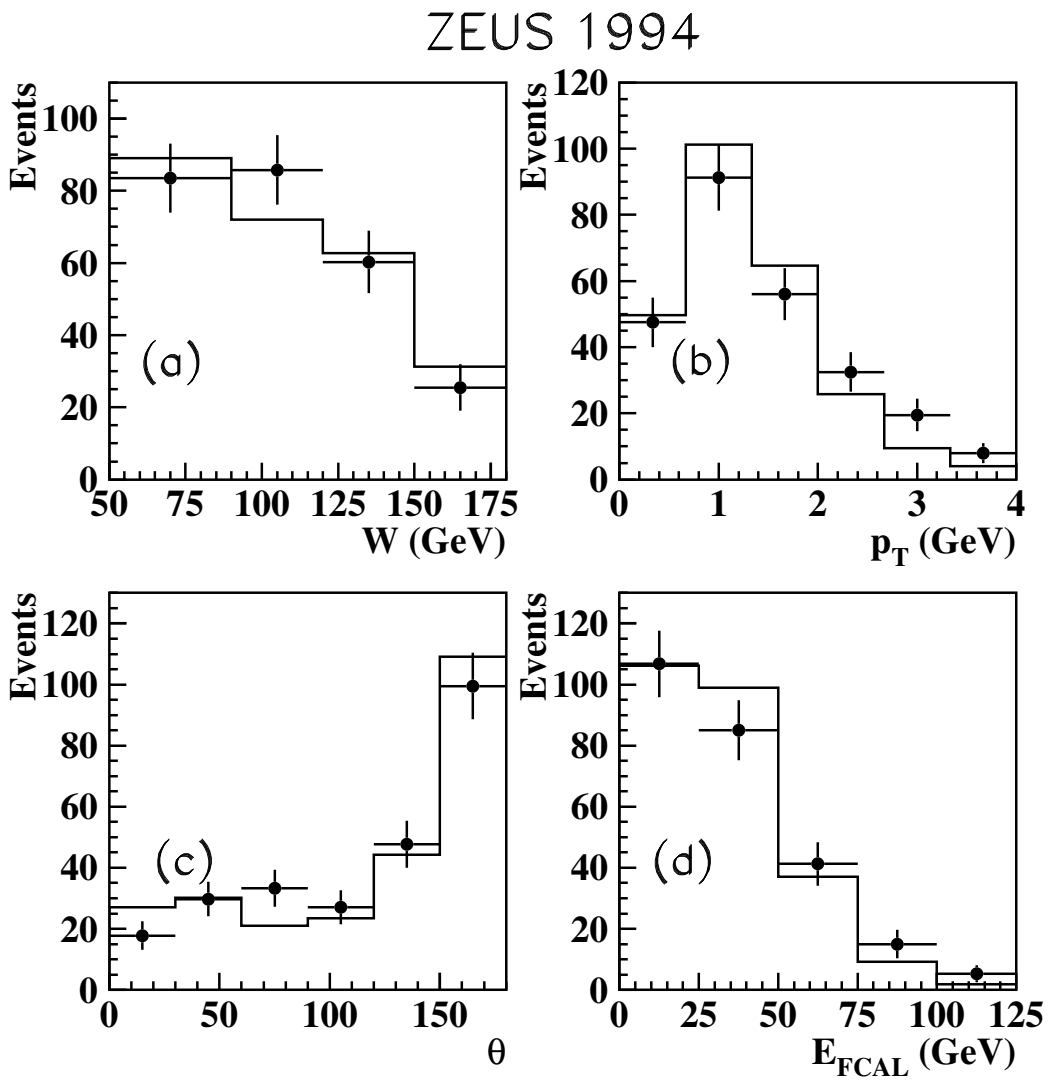

Figure 3: In (a) the uncorrected W distribution of the $\mu^+\mu^-$ data (full dots) with $0.4 < z < 1$ is compared to the mixture of HERWIG and EPSOFT (continuous histogram) described in section 5. In (b), (c) and (d) similar comparisons between data and the Monte Carlo mixture are shown for the distributions of p_T and polar angle θ of the J/ψ and for the energy in the forward calorimeter E_{FCAL}, respectively. The Monte Carlo mixture is normalized to the number of measured events.

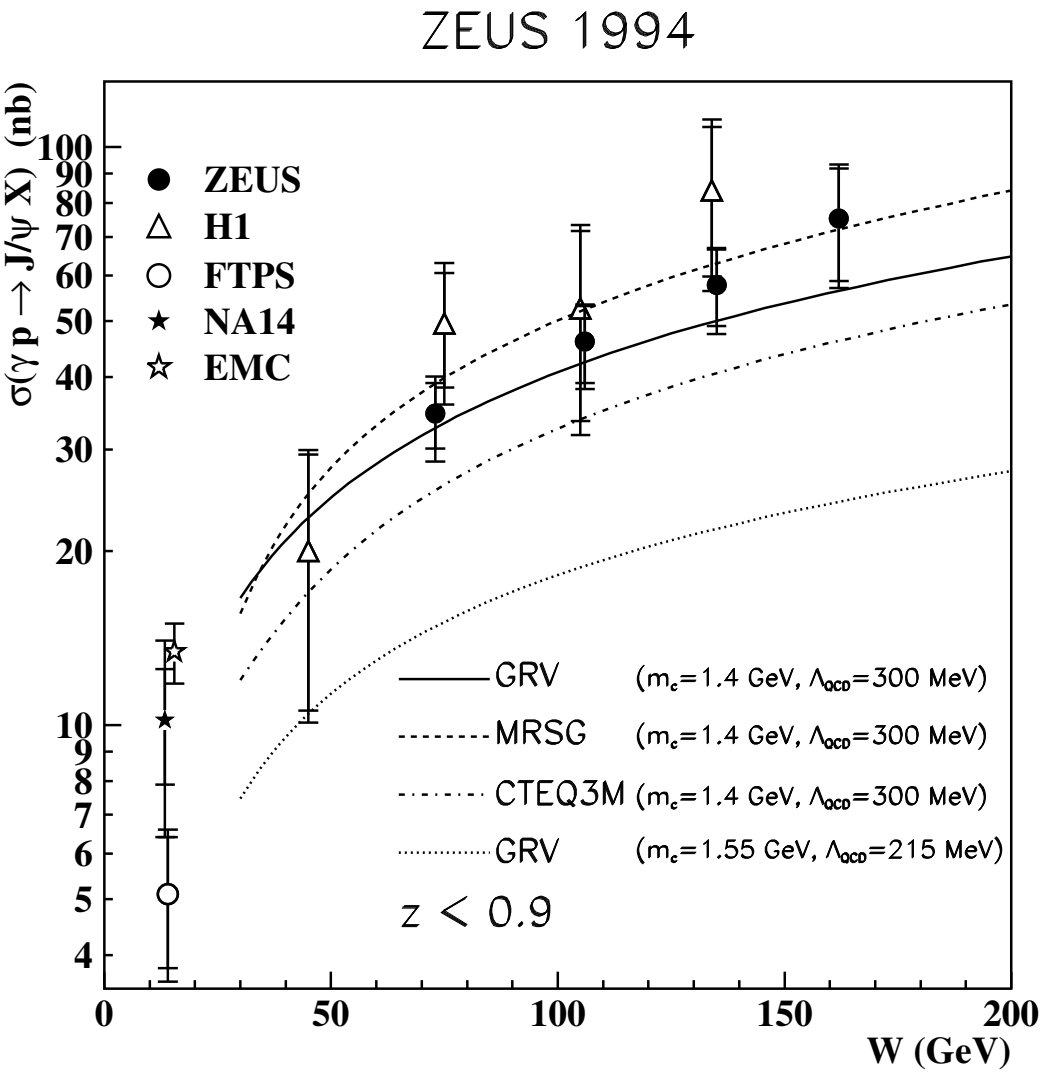

Figure 4: The direct inelastic J/ψ photoproduction cross section as a function of W for $z < 0.9$. Data from ZEUS, H1 [15], FTPS [9], NA14 [10] and EMC [14] are shown. The ZEUS result at the lowest W value is obtained with the muon channel only. The inner error bar indicates the statistical uncertainty, the outer error bar the quadratic sum of the statistical and systematic uncertainties. This is also true for the results from H1, FTPS and EMC Collaborations. The other three ZEUS measurements come from the combination of the electron and muon results as described in the text. The inner error bars represent the statistical and decay channel specific errors added in quadrature, the outer ones the statistical, decay specific and common systematic errors added in quadrature. The lines correspond to the NLO prediction from [1] assuming the GRV [27] (continuous), MRSG [30] (dashed) and CTEQ3M [34] (dotted-dashed) gluon distributions with $m_c = 1.4$ GeV and $\Lambda_{QCD} = 300$ MeV, the dotted curve was obtained with GRV, $m_c = 1.55$ GeV and $\Lambda_{QCD} = 215$ MeV . The curves are scaled up by a factor of 1.15 to take into account the contribution from $\psi' \to \mathrm{J}/\psi X$.

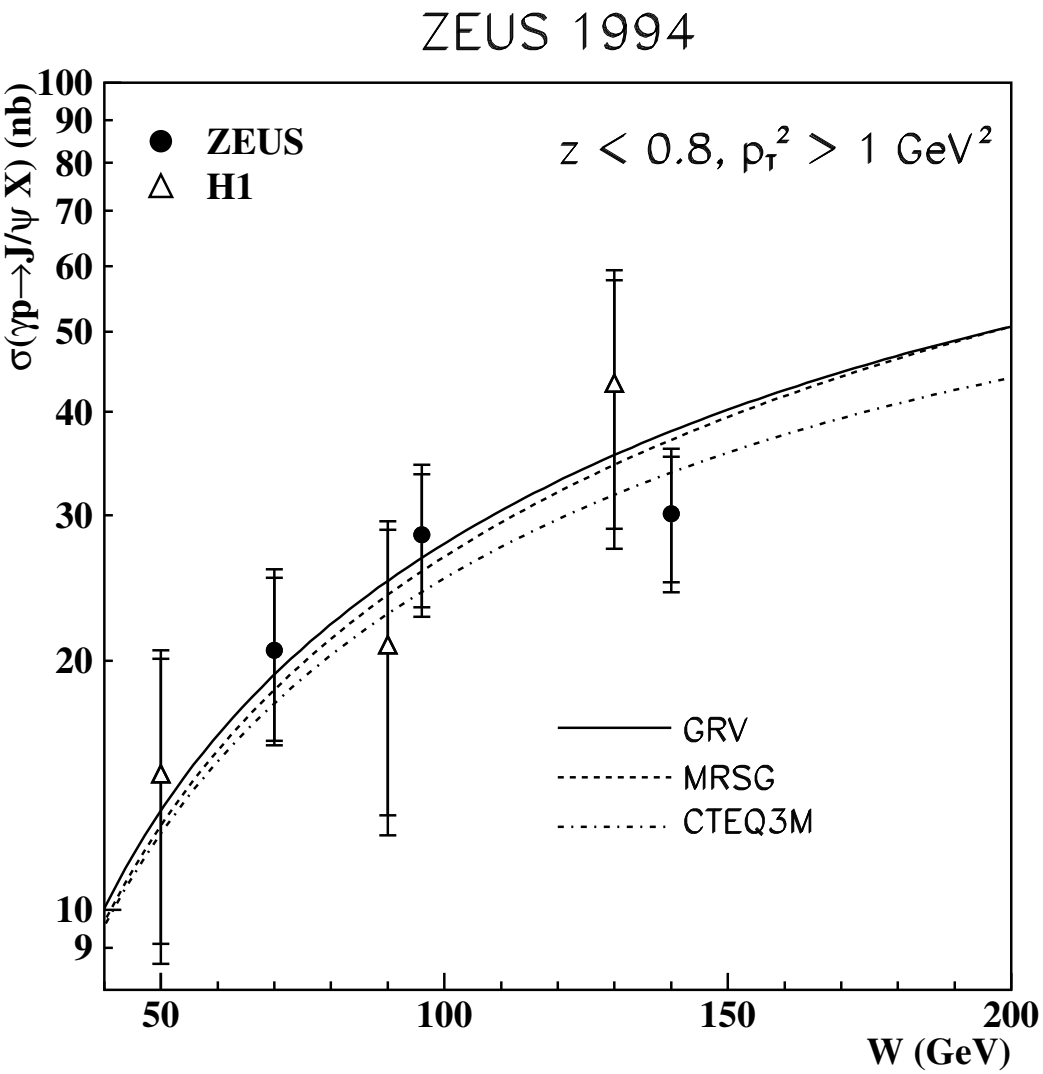

Figure 5: The direct inelastic J/ψ photoproduction cross section as a function of W for $z < 0.8$ and $p_T^2 > 1$ GeV^2. Data from ZEUS and H1 [15] are shown. The ZEUS results in the lowest two W bins are obtained with the muon channel only. The inner error bars indicate the statistical uncertainties, the outer error bars the quadratic sum of the statistical and systematic uncertainties. This is also true for the results from the H1 Collaboration. The ZEUS measurement in the highest W bin comes from the combination of the electron and muon results as described in the text. The inner error bar represents the statistical and decay channel specific errors added in quadrature, the outer one the statistical, decay specific and common systematic errors added in quadrature. The lines correspond to the NLO prediction from [1] assuming the GRV [27] (continuous), MRSG [30] (dashed) and CTEQ3M [34] (dotted-dashed) gluon distributions with $m_c = 1.4$ GeV and $\Lambda_{QCD} = 300$ MeV. The curves are scaled up by a factor of 1.15 to take into account the contribution from $\psi' \to$ J/ψX.

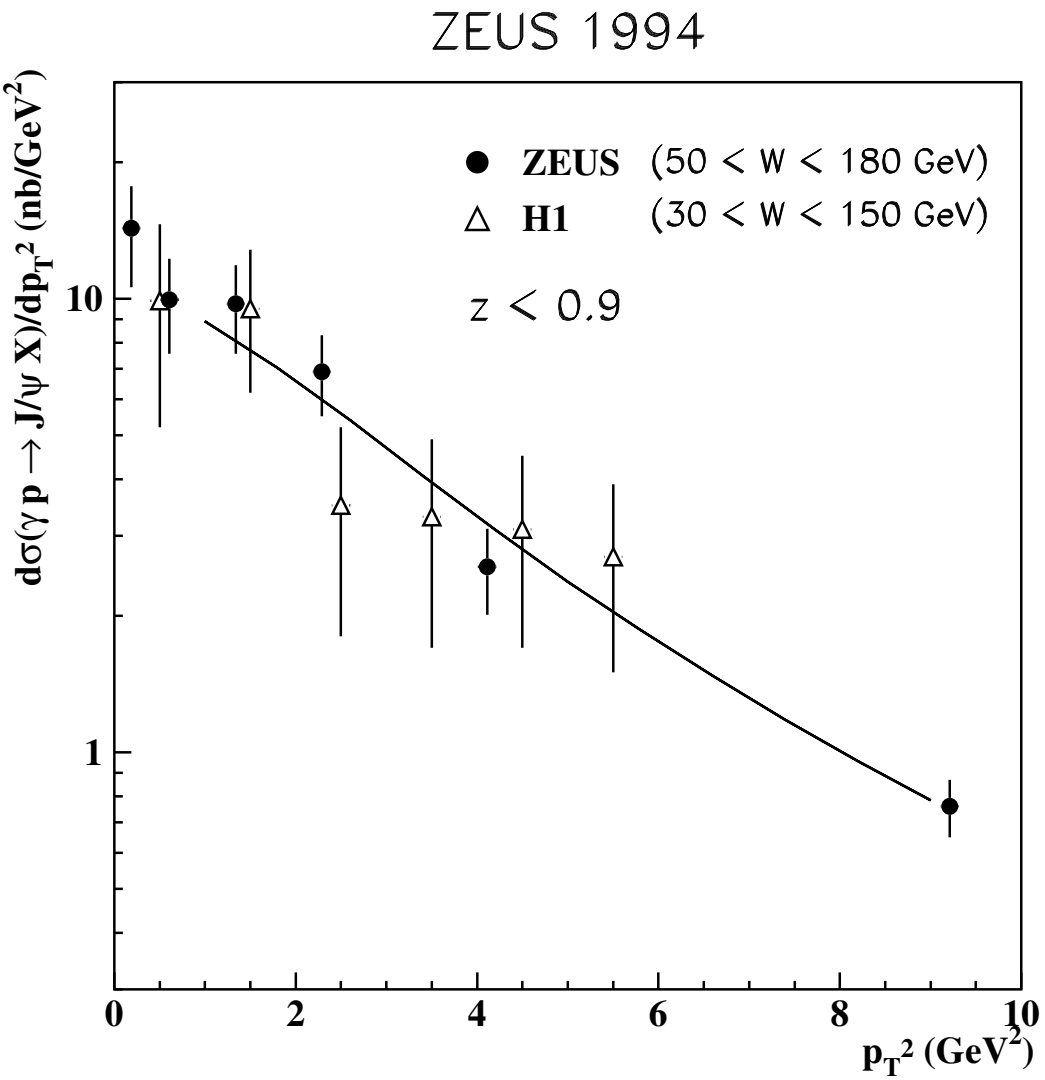

Figure 6: Differential cross section $d\sigma/dp_T^2$ for the inelastic $J/\psi \to \mu^+\mu^-$ sample with $50 < W < 180$ GeV and $z < 0.9$. Data from ZEUS and H1 [15] are shown. The error bars indicate the quadratic sum of the statistical and systematic uncertainties. The NLO computation [1] with the GRV [27] structure function, $m_c = 1.4$ GeV and $\Lambda_{QCD} = 300$ MeV is shown as the solid line. The theoretical curve is drawn only for $p_T^2 > 1$ GeV^2 because in the low p_T region the calculation is not reliable. In the theoretical curve the 15% contribution of the ψ' has not been included.

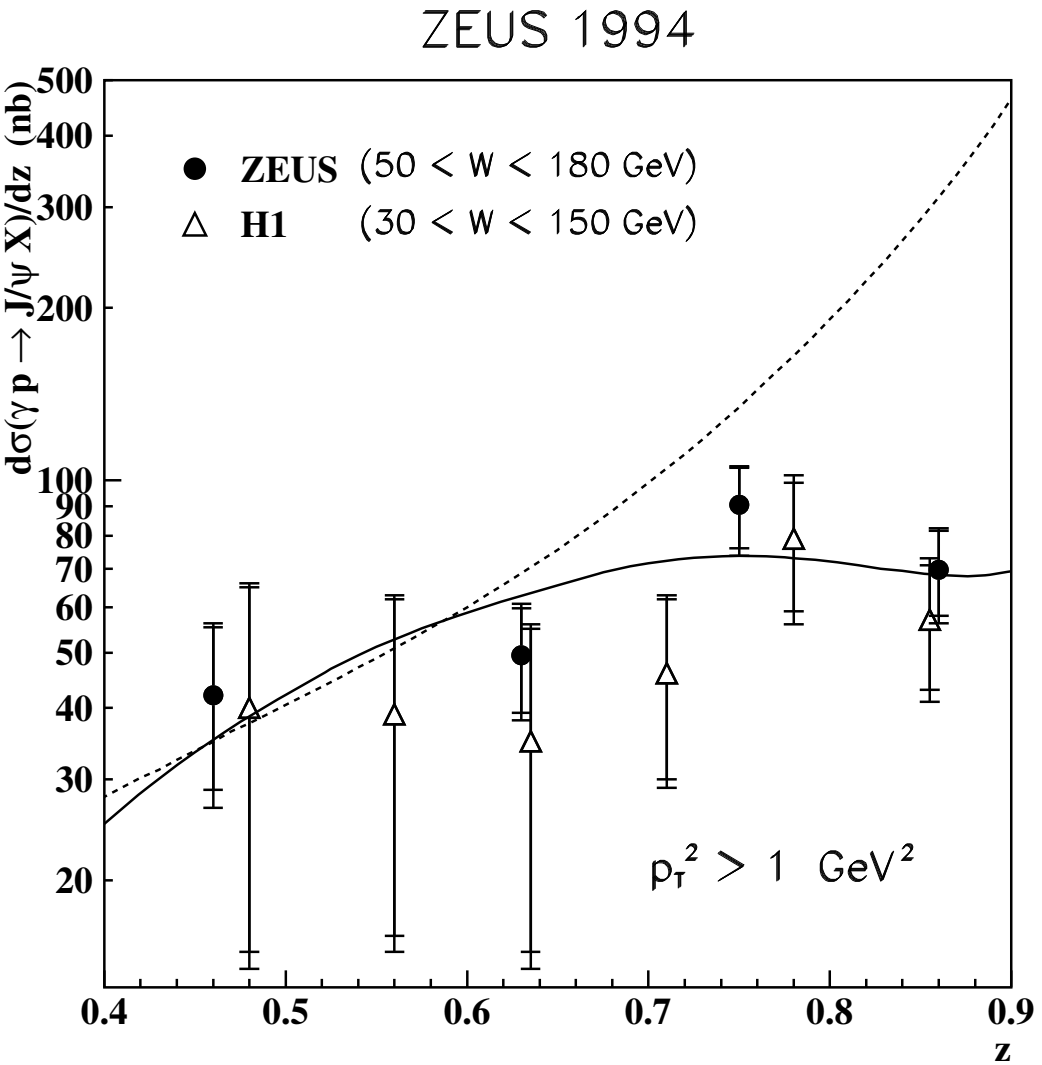

Figure 7: Differential cross section $d\sigma/dz$ for the inelastic $J/\psi \to \mu^+\mu^-$ sample with $50 < W < 180$ GeV and $p_T^2 > 1$ GeV^2. Data from ZEUS and H1 [15] are shown. The inner error bars indicate the statistical uncertainties, the outer error bars the quadratic sum of the statistical and systematic uncertainties. The NLO computation [1] with the GRV [27] structure function, $m_c = 1.4$ GeV and $\Lambda_{QCD} = 300$ MeV is shown as a solid line. The dashed line is given by the sum of the colour-singlet and the colour-octet leading order calculations [8]. In the theoretical curves the 15% contribution of the ψ' has not been included.